Symmetry breaking and unconventional charge ordering in single crystal Na$_{2.7}$Ru$_4$O$_9$

Arvind Yogi,[1,2,*] C. I. Sathish,[1,2] Hasung Sim,[1,2] Matthew J. Coak,[1,2] Y. Noda,[3,4] and Je-Geun Park[1,2,†]

[1]*Center for Correlated Electron Systems, Institute for Basic Science (IBS), Seoul 08826, Korea*

[2]*Department of Physics and Astronomy, Seoul National University, Seoul 08826, Korea*

[3]*J-PARC center, Institute of Materials Structure Science, High Energy Accelerator Research Organization (KEK), Tsukuba, Ibaraki 305-0801, Japan*

[4]*Institute of Multidisciplinary Research for Advanced Materials, Tohoku University, Sendai 980-8577, Japan*

The interplay of charge, spin, and lattice degrees of freedom in matter leads to various forms of ordered states through phase transitions. An important subclass of these phenomena of complex materials is charge ordering (CO), mainly driven by mixed-valence states. We discovered by combining the results of electrical resistivity (ρ), specific heat, susceptibility (χ), and single crystal x-ray diffraction (SC-XRD) that Na$_{2.7}$Ru$_4$O$_9$ with the monoclinic tunnel type lattice (space group $C2/m$) exhibits an unconventional CO at room temperature while retaining metallicity. The temperature-dependent SC-XRD results show successive phase transitions with superlattice reflections at $\mathbf{q}_1 = (0, \frac{1}{2}, 0)$ and $\mathbf{q}_2 = (0, \frac{1}{3}, \frac{1}{3})$ below T_{C2} (365 K) and only at $\mathbf{q}_1 = (0, \frac{1}{2}, 0)$ between T_{C2} and T_{C1} (630 K). We interpreted these as evidence for the formation of an unconventional CO. It reveals a strong first-order phase transition in the electrical resistivity at T_{C2} (cooling) = 345 K and T_{C2} (heating) = 365 K. We argue that the origin of the phase transition is due to the localized $4d$ Ru electrons. The results of our finding reveal an unique example of Ru^{3+}/Ru^{4+} mixed valance heavy d^4 ions.

I. INTRODUCTION

Symmetries are important in condensed matter systems with strong ramifications on physical properties. Phase transitions are usually accompanied by a broken symmetry [1], which then leads to the appearance of some ordered phases [2]. In solids, the conduction electrons experience competing interactions with each other and with elementary excitations. Ru-based materials have recently emerged as a fertile ground for emergent phenomena driven by a modest spin-orbit coupling (SOC) typical of $4d$ electronic states [3–10]. The $4d$ electrons of Ru are also known to exhibit both localized and itinerant characters. A subtle balance between localization and itinerancy commonly gives rise to a rich variety of electronic and magnetic properties [11].

The heavy d^4 ions based systems have been widely investigated, particularly because of interplay between SOC with intermediate strength ($\simeq 0.16$ eV) and Coulomb interaction U. This competition appears to lead to numerous unusual properties with several interesting examples: unconventional superconductivity [12], metal-insulator transitions [13–15], orbital ordering [5], non-Fermi liquid behavior [16,17], high-temperature ferromagnetism [18], low-temperature p-wave spin-triplet superconductivity [19], electron nematic behavior [20,21], quantum criticality [9,22], and itinerant ferro- and metamagnetism [23,24]. Furthermore, the tunnel-type structures such as Rutile, Ramsdellite and Hollandite can accommodate valencies from $+2$ to $+5$ [25,26] and mixed valencies lead to several interesting phenomena such as charge, spin, and

orbital ordering [27–29]. In this context, Na$_{2.7}$Ru$_4$O$_9$ (large tunnel type structure) is a promising material for investigating the interplay between Coulomb interactions and the modest SOC of the mixed valance heavy d^4 ions.

Among the competing phases, charge ordering is direct evidence of the Coulomb interaction. When the Coulomb interaction is the dominant energy scale, systems tend to be more localized. In this localized state, one often finds an insulating phase with a certain charge ordering (CO). However, this CO becomes unstable as one raises the itinerancy by increasing bandwidth (W) or reducing the relative effects of the Coulomb U. This relative ratio of W and U gives rise to two routes to the metal-insulator transition (MIT): one is a bandwidth controlled MIT and the other is Mott-Hubbard MIT. It is generally believed that regardless of the two mechanisms of MIT the CO disappears when the system becomes metallic, with examples found in $3d$ transition metal oxides. However, it is not entirely clear how this picture should change with the introduction of spin-orbit coupling. In this sense, it is very important to accumulate enough experimental data before reaching at least some kind of phenomenological understanding of CO and related MIT for $4d$ or $5d$ transition metal oxides (TMO), where the spin-orbit interaction is stronger.

Na$_{2.7}$Ru$_4$O$_9$ crystallizes in a monoclinic crystal structure with a large tunnel running parallel to the crystallographic b axis. The structure consists of corner and edge sharing RuO$_6$ octahedra arranged in one-dimensional zigzag chains, which are formed by single, double, and triple edge shared chains, respectively. These zigzag chains are linked together parallel to the c axis by their corners. In this report, we present physical properties in a wide temperature range (1.9 K $\leqslant T \leqslant$ 450 K) using single crystals. We studied the structural, electronic, and magnetic properties of the mixed valence Ru^{3+}/Ru^{4+}

*yogi.arvind2003@gmail.com

†jgpark10@snu.ac.kr

compound $Na_{2.7}Ru_4O_9$ and report CO behavior without the loss of metallicity.

II. METHODS

Polycrystalline $Na_{2.7}Ru_4O_9$ samples were synthesized by solid state reaction of preheated RuO_2 (99.999%, Aldich) and Na_2CO_3 (99.999%, Aldich) under an Ar-gas environment at 900 °C for 72 h with several intermediate grindings and pelletizations. Subsequently, high-quality single crystals of $Na_{2.7}Ru_4O_9$ were grown from this polycrystalline powder via a modified self-flux vapor transport reaction under flowing Ar gas (ultra-pure 99.999%). Long needle shaped high-quality single crystals ($1 \times 0.1 \times 0.1$ mm^3) were obtained from the final products.

The phase purity and temperature-dependent (300 to 450 K) powder XRD patterns were collected using a Bruker D8 Discover diffractometer with a Cu-K$_\alpha$ source with no impurity peaks observed. An elemental analysis was subsequently done confirming the stoichiometry of the samples: We used a COXI EM-30 scanning electron microscope equipped with a Bruker QUANTAX 70 energy dispersive x-ray system. The temperature-dependent single crystal XRD (SC-XRD) was performed from 300 to 695 K by using a single crystal diffractometer (XtaLAB P200, Rigaku). The crystal structure was refined using both powder and single crystal XRD data with the FULLPROF [30] software suite.

Electrical resistivity (ρ) measurements were carried out using a homemade system equipped with a furnace (300 to 450 K) and a pulsed-tube cryostat (down to 3 K, Oxford). The electrical resistance was measured in the four-point geometry on a static sample holder, where the contacts to the sample were made using silver paint and 25 μm gold wire. Current (I) was applied perpendicular to the single crystal length, which is the crystallographic b axis. Magnetic susceptibility $\chi(T)$ measurements were taken using a MPMS-SQUID magnetometer (Quantum Design). Heat capacity $C_p(T)$ measurements were made using the commercial physical property measurement system (PPMS, Quantum Design).

III. RESULTS

A. Electrical resistivity, heat capacity, and magnetization

Electrical resistivity is shown for single crystal $Na_{2.7}Ru_4O_9$ in Fig. 1(a) in the temperature range of 3.3 K $\leqslant T \leqslant$ 450 K for both heating and cooling cycles. Metallic conductivity ($d\rho/dT > 0$) is observed in the entire temperature range with a room temperature resistivity of 187 $\mu\Omega$ cm. The electrical resistivity reveals a clear hysteresis, indicative of a first-order phase transition with two transitions at T_{C2} (cooling) = 345 K and T_{C2} (heating) = 365 K, which is corroborated well by magnetization and heat-capacity results (Fig. 1). However, no significant difference could be observed for the resistivity up to 9 T as compared with the zero field resistivity. On the other hand, above T_{C2} we observed negative $d\rho/dT$ and a small sign of saturation. The most probable reason for this is the scattering process of the conduction electrons due to a narrow band (d band) in the proximity of the Fermi energy. In order to shed light on the scattering mechanism involved and to have a quantitative understanding of the measured results, the electrical
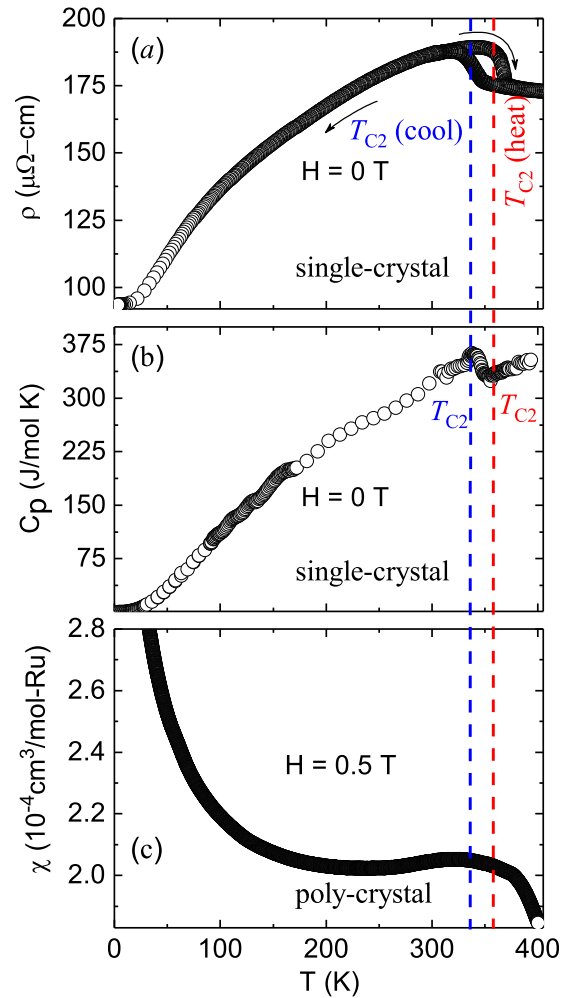

FIG. 1. The first order phase transition is observed at T_{C2} (cooling) = 345 K and T_{C2} (heating) = 365 K, with a clear hysteresis in resistivity (ρ) upon warming and cooling (a), which is also evident in specific heat (C_p) (b) and in magnetic susceptibility $\chi(T)$ of $Na_{2.7}Ru_4O_9$ (c).

resistivity data of $Na_{2.7}Ru_4O_9$ was analyzed theoretically by using a Bloch-Grüneisen-Mott model [31]. Using this model, we can show that the temperature dependence of the resistivity can be explained by the electron-phonon and interband electron mediated scattering mechanisms (see Supplemental Material (SM-1) and Fig. S1 [32]).

Our theoretically estimated ρ values are consistent with the experimental data for $Na_{2.7}Ru_4O_9$. Parameters derived from the Bloch-Grüneisen-Mott (BGM) model (4.2 K $\leqslant T \leqslant$ 300 K) are the characteristic Debye temperature (Θ_ρ) = 140.6 K, residual resistivity (ρ_0) = 94$\mu\Omega$ cm, and Mott's s-d interband electron scattering constant (K) = 5$\mu\Omega$ cm/K^3. However, the clear differences in the linear slope of the resistivity with temperature indicate phonon softening. In order to describe this resistivity behavior theoretically, we considered an additional s-d interband electron scattering. The lower value of Θ_ρ can be attributed to lattice softening and localized lattice vibrations because of the Na and Ru atom displacements as discussed in detail in the next section. Moreover, the estimated Debye temperature $\Theta_D = \sqrt[3]{(12 \times \pi^4 N \times R)/5\beta}$, for $Na_{2.7}Ru_4O_9$, obtained from a β value of 3.7×10^{-4} J/mol K^4 (low temperature heat capacity fit), is found to be $\Theta_D = 444$ K,

which is significantly different from Θ_ρ. One probable reason for this discrepancy is that the heat capacity is more evenly affected by both the acoustic and optic modes of phonons whereas BGM resistivity is preferentially dominated by the optic mode, and therefore Θ_D and Θ_ρ are not necessarily expected to be equal [33]. Further, the Debye temperature Θ_D is found to be very close to that of other ruthenium based non-Fermi-liquid compound $CaCu_3Ru_4O_{12}$ where $\Theta_D = 451$ K [34].

Heat capacity for $Na_{2.7}Ru_4O_9$ was measured in the temperature range 1.9 K $\leqslant T \leqslant 400$ K and is displayed in Fig. 1(b). The specific heat shows two strong kinks with an inflection point at T_{C2} (cooling) = 345 K and T_{C2} (heating) = 365 K as shown by dashed lines in Fig. 1(b). The sharp feature of the peak, different from the usual lambdalike shape, confirms a first-order transition in $Na_{2.7}Ru_4O_9$. The absence of a clear sign of magnetic ordering in the susceptibility shown in Fig. 1(c) indicates that a structural transition is most likely responsible for the observed hysteresis in the resistivity. The low temperature heat capacity data can be analyzed in terms of

$$C_P = \gamma T + \beta T^3, \tag{1}$$

where γ is the electronic specific heat coefficient and β is the phonon contribution to the total specific heat [35]. The evidence for a metal-like electronic contribution to the low-temperature heat capacity was observed. The electronic contribution to the specific heat (γ) for $Na_{2.7}Ru_4O_9$ was determined to be 26 mJ/mol K^2, indicating an enhanced contribution of conduction electrons in excellent agreement with the transport measurements. The extracted phonon contribution (β) from the equation (1) is found to be 3.7×10^{-4} J/mol K^4, which is similar to the reported value of β for $CaCu_3Ru_4O_{12}$ [34]. Moreover, the estimated value of γ for $Na_{2.7}Ru_4O_9$ is much larger than the free electron value of γ and comparable with the values for other ruthenates: e.g., Ru superconductor Sr_2RuO_4 ($\gamma = 40$ mJ/mol K^2 Ru) and non-Fermi-liquid compound $La_4Ru_6O_{19}$ ($\gamma = 25$ mJ/mol K^2 Ru) [17,19]. This large value of γ indicates that the conduction electrons, most likely from Ru $4d$ bands, are strongly correlated. Further, using the relation between heat capacity

and latent heat $l = C \times \Delta T$, we estimated the latent heat at the first order phase transition to be 722.9 J/mol.

Bulk magnetic susceptibility (χ) for $Na_{2.7}Ru_4O_9$ was measured as a function of temperature in the temperature range 1.9 K $\leqslant T \leqslant 400$ K under an applied field of 0.5 T using a polycrystalline sample as shown in Fig. 1(c). Magnetization as a function of applied field (H) was measured at 2 and 400 K, and exhibits linear variation without any hysteresis within a maximum applied field of 7 T. For practical reasons, we measured magnetization using a large mass of crushed powder sample. The magnetic susceptibility (1.9 K $\leqslant T \leqslant 400$ K) of the compound is temperature independent from room temperature to 150 K, indicative of Pauli-paramagnetic behavior, which is followed by a Curie-like increase at lower temperature. Notably, the susceptibility curve above room temperature demonstrates a broad hump at the first order phase transition as seen in Fig. 1(c). This is probably due to short range correlations present at such high temperatures. The temperature dependence of the inverse susceptibility in a field of 0.5 T is highly nonlinear. The effective magnetic moment (μ_{eff}), and the Curie-Weiss temperature (θ_{CW}), determined from the modified Curie-Weiss fit to the experimental data and are found to be $\theta_{CW} = -11.9$ K and $\mu_{eff} = 0.18 \mu_B$, respectively [see Supplemental Material (SM-3) and Fig. S2]. Above the first order phase transition, magnetic susceptibility drops drastically, showing the loss of conduction electrons and eventually as increase in localized electrons, further confirming the reported scenario for Na deficient $Na_{3-x}Ru_4O_9$ from Na-NMR experiments [37].

We must note that bulk properties of $Na_{2.7}Ru_4O_9$ are significantly different from $Na_2Ru_4O_{9-\delta}$, which shows large anisotropy in both resistivity and magnetic susceptibility (χ). The metallic as well as magnetic behavior of $Na_2Ru_4O_{9-\delta}$ was attributed to the presence of localized as well as itinerant Ru electrons [36].

B. X-ray diffraction measurements

In order to understand the origin of the phase transition observed in the electrical resistivity and heat capacity data, we
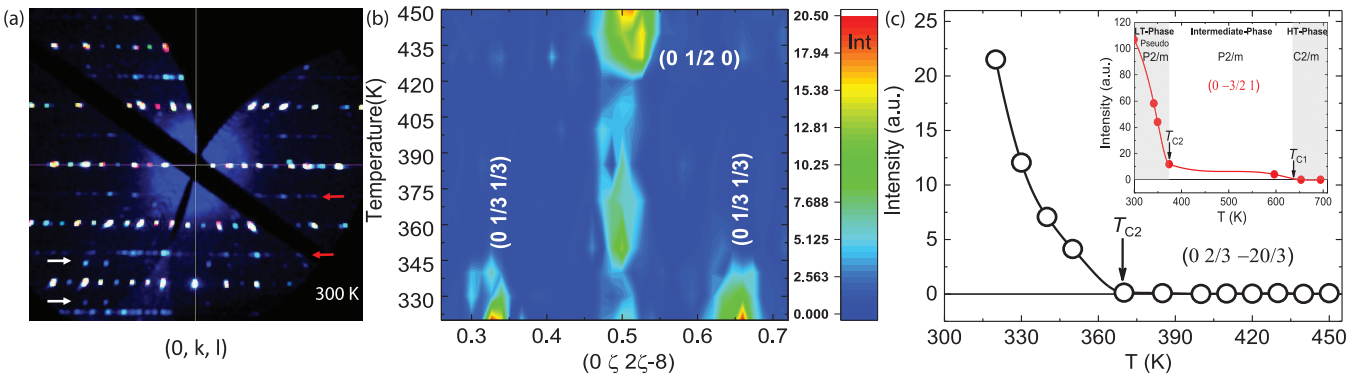

FIG. 2. (a) Reciprocal lattice map of the SC-XRD data for $Na_{2.7}Ru_4O_9$ measured at 300 K below the first order transition temperature T_{C2}. The fundamental $(0,k,l)$ reflections (white spots) and the weak satellite reflections corresponding to superlattice peaks at $\mathbf{q}_1 = (0, \frac{1}{2}, 0)$ and $\mathbf{q}_2 = (0, \frac{1}{3}, \frac{1}{3})$ in the b^*-c^* plane, marked by red and white arrows, respectively. (b) Line cuts through superlattice peaks $\mathbf{q}_1$ and $\mathbf{q}_2$ for various temperatures below and above the first order transition as extracted from the reciprocal image. (c) Temperature dependence of the $\mathbf{q}_2$ superlattice peaks. The $\mathbf{q}_2$ peak disappears above the first order transition ($> T_{C2}$) ≈ 370 K. Above T_{C2}, only the $\mathbf{q}_1$ superlattice peak was observed; this eventually disappears above T_{C1} as shown in the inset.

performed multiple diffraction experiments on single crystal and polycrystalline $Na_{2.7}Ru_4O_9$ in the temperature range between 300 and 695 K. Interestingly enough the temperature-dependent SC-XRD results show successive phase transitions. For example, a single superlattice peak appears at $\mathbf{q}_1 = (0, \frac{1}{2}, 0)$ in the intermediate phase ($T_{C1} \equiv 630$ K), whereas two superlattice peaks emerge at $\mathbf{q}_1 = (0, \frac{1}{2}, 0)$ and $\mathbf{q}_2 = (0, \frac{1}{3}, \frac{1}{3})$ below T_{C2} in the LT phase as shown in Figs. 2(a) and 2(b). We note that these superlattice peaks were not reported in the previous study [35] on powder samples, most probably due to weak reflections.

In addition, the superlattice peak at $\mathbf{q}_2 = (0, \frac{1}{3}, \frac{1}{3})$ disappears on heating as shown in Figs. 2(b) and 2(c). The line cut from the temperature-dependent reciprocal image analysis for the peak $\mathbf{q}_2 = (0, \frac{1}{3}, \frac{1}{3})$ shows a clear suppression of intensity above T_{C2} [Fig. 2(c)]. This behavior is similar to that observed in Na deficient $Na_{3-x}Ru_4O_9$ [37], where Na^+-NMR spectra results show motional averaging of the Na^+ sites at 390 K (above the first order phase transition). According to Ref. [37], this motional averaging of the Na^+ sites was discussed in the context of the ionic motion in the material. Above 360 K the ordered state begins to melt rapidly, consistent with our transport results. This suggests a large variation in the charge separation patterns in a mixed valance system below and above the melting of the ordered state (see Section: Crystal-structure analysis).

The superlattice spots indicate that the observed modulations in $Na_{2.7}Ru_4O_9$ are commensurate ($\mathbf{q}_1 = (0, \frac{1}{2}, 0)$ and $\mathbf{q}_2 = (0, \frac{1}{3}, \frac{1}{3})$) superstructure type with translation and rotational symmetry breaking. Interestingly, this symmetry breaking induces large ionic displacements (Na ions) in the lattice, which can be explained by a monoclinic structure with the subgroup of $C2/m$. This $C2/m$ unit cell doubles the cell ($a_0 \times 2b_0 \times c_0$) with $\mathbf{q}_1 = (0, \frac{1}{2}, 0)$ below 630 K and with further cooling makes the cell 18 times larger ($a_0 \times 6b_0 \times 3c_0$) with another $\mathbf{q}_2 = (0, \frac{1}{3}, \frac{1}{3})$ from the prototype HT phase. The schematic diagrams of the reciprocal unit cell are shown in Fig. 3 at room temperature [$\mathbf{q}_1 = (0, \frac{1}{2}, 0)$ and $\mathbf{q}_2 = (0, \frac{1}{3}, \frac{1}{3})$], at 450 K [$\mathbf{q}_1 = (0, \frac{1}{2}, 0)$] and above the T_{C1} at 695 K with reciprocal lattice maps, respectively. The mirror and twofold symmetry were not observed in the SC-XRD data in the LT phase (300 K). Therefore we can conclude that the observed Laue symmetry should be $P\bar{1}$.

Further, the superlattice peak at $\mathbf{q}_1 = (0, \frac{1}{2}, 0)$ appears at T_{C1} and suddenly increases again below T_{C2} as shown in the inset of Fig. 2(c). The observed behavior of this superlattice peak reflects the large displacements of Na ions below T_{C2} (see Section: Displacement pattern). However, it is generally believed that such weak additional satellite reflections are due to the presence of various types of charge density wave (CDW) or CO states in tunnel type structures such as Hollandite $A_xM_8O_{16}$ [26].

C. Crystal-structure analysis

The crystal structure of $Na_{2.7}Ru_4O_9$ has been investigated at intermediate temperature (450 K) and room temperature (300 K) SC-XRD as shown in Figs. 4(a) and 4(b) and further confirmed by powder-XRD measurements Figs. 4(c) and 4(d). We failed to obtain reliable intensity data at HT phase because
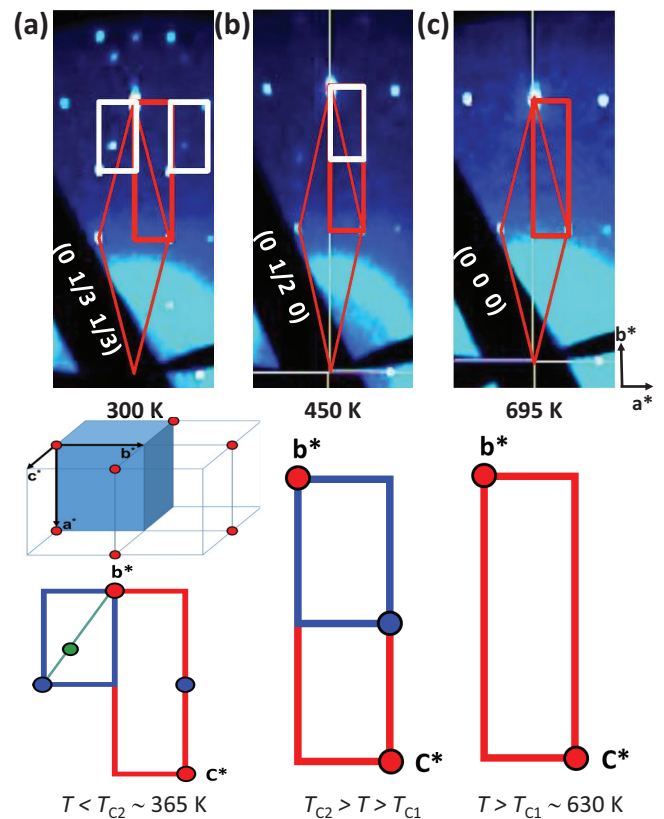

FIG. 3. Schematic diagrams of the reciprocal unit cell at the LT phase at 300 K (a) and at the intermediate phase at 450 K (b) including superlattice peaks at $\mathbf{q}_1 = (0, \frac{1}{2}, 0)$ and $\mathbf{q}_2 = (0, \frac{1}{3}, \frac{1}{3})$ as observed in SC-XRD measurements. The SC-XRD data with schematic diagrams above T_{C1} at the final HT phase at 695 K (c), where no superstructure reflections were observed (prototype $\equiv C2/m$). The unit cell of the LT phase (300 K) and the intermediate phase (450 K) becomes ($a_0 \times 6b_0 \times 3c_0$) and ($a_0 \times 2b_0 \times c_0$), respectively, as compared to the prototype HT-phase $C2/m$ unit cell ($a_0 \times b_0 \times c_0$).

the samples decomposed as a long time experiment. We observed a single superlattice peak with $\mathbf{q}_1 = (0, \frac{1}{2}, 0)$ for the intermediate phase (450 K) and two superlattice peaks with $\mathbf{q}_1 = (0, \frac{1}{2}, 0)$ and $\mathbf{q}_2 = (0, \frac{1}{3}, \frac{1}{3})$ for the LT phase (300 K) in the SC-XRD data (Fig. 3). These superlattice peaks can be indexed by using the monoclinic space group $C2/m$ of the prototype HT phase. Under the group-subgroup relation, $P2/m$ is assigned to the intermediate $\mathbf{q}_1 = (0, \frac{1}{2}, 0)$ phase. The $\mathbf{q}_2 = (0, \frac{1}{3}, \frac{1}{3})$ superlattice reflection leads to a significant increase of the unit cell volume and lowers the symmetry drastically at room temperature. To explain the $\mathbf{q}_1 = (0, \frac{1}{2}, 0)$ superlattice peak for the intermediate phase at 450 K, $P2/m$ symmetry was used to refine the SC-XRD data under the group-subgroup relation by taking atomic positions from the earlier report on powder samples [35] at room temperature with a $C2/m$ space group (corresponding to the prototype HT phase, >630 K). The structure of the room temperature phase with $\mathbf{q}_1 = (0, \frac{1}{2}, 0)$ and $\mathbf{q}_2 = (0, \frac{1}{3}, \frac{1}{3})$ is more complicated. From the observed Laue symmetry, we conclude that the space group should be $P\bar{1}$, but there are too many fitting parameters. Thus, we ignored the $\mathbf{q}_2 = (0, \frac{1}{3}, \frac{1}{3})$ superlattice reflections and made an averaged structure analysis with the same unit-cell size and
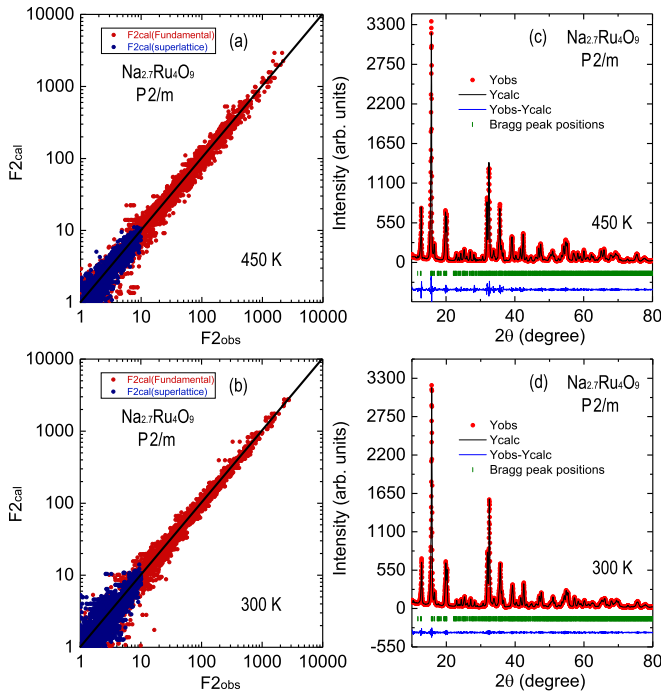
FIG. 4. The left panel shows plots for F^2-obs and F^2-cal for single crystal experiments at (a) 450 and (b) 300 K, respectively. Red markers represent fundamental reflections, while blue markers represent superlattice reflections. Note that the vertical and horizontal axis are given in a logarithmic scale. The right panel shows Le-Bail refined x-ray powder diffraction patterns at (c) 450 and (d) 300 K, respectively. Blue line at the bottom of each panel in (c) and (d) represents the difference between F-cal and F-obs.

FIG. 5. The projection of the crystal structure of $Na_{2.7}Ru_4O_9$ is the intermediate phase (450 K) (bottom panel) and the LT phase (300 K) (top panel) in the crystallographic ac plane. The unit cell at 300 K is simply tripled from the analyzed cell on drawing. BVS calculations at 450 and 300 K show the segregation of Ru valence as Ru^{3+} (green)/Ru^{4+} (light brown) RuO_6 octahedra. The typhoonlike lager red mark represents a screw-axis symmetry of monoclinic $P2/m$ remaining under group-subgroup relation.

the same space group $P2/m$ of the intermediate phase as an approximant structure. The obtained R factors (R_{F2}) for the intermediate and LT phases are 11.41 and 16.01, respectively [see Figs. 4(a) and 4(b)]. The refined lattice parameters for the prototype HT phase at 695 K, the intermediate phase at 450 K, and the LT phase at 300 K (room temperature) are shown in Table I.

The crystal structure of $Na_{2.7}Ru_4O_9$ for the intermediate and low (room) temperature phases is shown in Fig. 5. The structural parameters obtained from SC-XRD refinement are shown in Tables S1 and S2 (see SM-2) and were used as the starting point of powder HR-XRD structural refinements to double check our structural model. All Bragg reflections were well indexed by assuming the monoclinic space group $P2/m$ and the HR-XRD refinement shows an excellent fit as shown
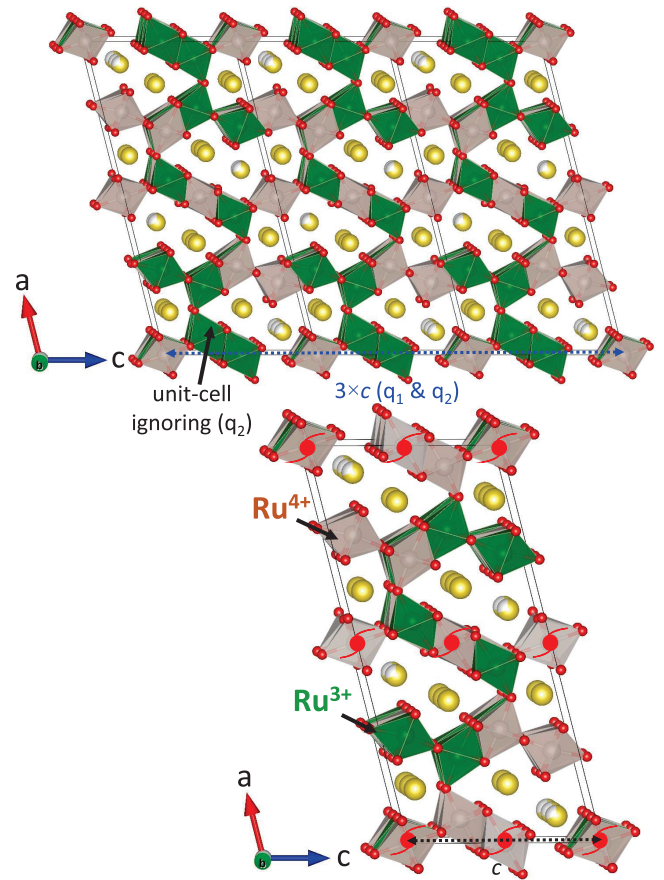
in Figs. 4(c) and 4(d). Note that superlattice reflections found by single-crystal experiments are too weak to be seen in the powder reflection profiles shown in Figs. 4(c) and 4(d).

To explain the crystal structure of $Na_{2.7}Ru_4O_9$ by considering the observed superstructures, we begin from the intermediate phase where a single superlattice peak (q_1) appears (bottom panel of Fig. 5) and then two superlattice peaks (q_1 and q_2) emerge in the room (low) temperature phase, which triples the cell parameters b and c of the unit cell (top panel

TABLE I. The unit-cell size and the space group of $Na_{2.7}Ru_4O_9$ for the HT phase [695 K ≡ Prototype $C2/m$], the intermediate phase [450 K ≡ $P2/m$], and the LT phase [300 K ≡ Pseudo $P2/m$ ($P\bar{1}$)] have been investigated by single crystal x-ray diffraction measurements. The obtained values of the lattice parameters for different phases are listed below. The numbers in the parentheses are the respective error.

Temperature	lattice parameters				
	a (Å)	b (Å)	c (Å)	β (°)	V (Å^3)
695 K	23.520 (11)	2.890 (1)	10.953 (6)	104.55(3)	720.6 (6)
450 K	23.311 (2)	5.701 (4)	11.057 (7)	104.39(4)	1423.3(2)
300 K	23.342 (2)	17.028 (16)	33.191 (3)	104.43(7)	12776.1(6)

of Fig. 5). The different types of RuO$_6$ octahedra of the corner sharing chains are comprised of single, double, or triple edge-shared chains of RuO$_6$ octahedra. It then has irregular zigzag chains of RuO$_6$ octahedra along the crystallographic c axis as well as large channels or cavities in the crystallographic ac plane, in which multiple Na$^+$ atoms can reside (Fig. 5). Interestingly, along the crystallographic b axis Na$_{2.7}$Ru$_4$O$_9$ forms a tunnel type structure, which is different from other prototype tunnel structures such as Rutile, Ramsdellite, or Hollandite-type [25,26] (see Section: Tunnel structure).

Furthermore, the associated bond valence sum (BVS) calculation was performed using the FULLPROF software suite [30], which reveals Ru^{3+} (green RuO$_6$ octahedron) and Ru^{4+} (light brown RuO$_6$ octahedron) coexisting in different valence states at both 300 and 450 K (Fig. 5). The change in Ru-O bond length for Ru^{4+} and Ru^{3+} varies dynamically and the charge ratio in a unit cell are found to be around 3:1 and 1:1 at 450 and 300 K, respectively. The electronic properties mainly depend on the charge, and charge separation is a common feature of charge ordering phenomena. At first sight, the emergence of the superlattice peaks can be interpreted as evidence of CO, such as in the case of tunnel based structure's like Hollandite-type [26] or in Na based compound Na$_x$CoO$_2$ with a Co^{3+}/Co^{4+} CO state [38]. These features, therefore, indicate that Na$_{2.7}$Ru$_4$O$_9$ has unconventional CO without the loss of metallicity at room temperature. Above the first order phase transition at T_{C2}, it also shows the CO state but below the first order phase transition at T_{C2}, the CO pattern drastically changes as shown in the lower panel of Fig. 5.

IV. DISCUSSION AND SUMMARY

A. Tunnel structure

The crystal structure of Na$_{2.7}$Ru$_4$O$_9$ is composed of irregular zigzag chains forming tunnels along the b axis. The Na ions are located inside these tunnels at three different crystallographic sites. However, a large number of Na$^+$ cations inside the tunnel experience strong mutual electrostatic repulsion and that increases as a function of temperature as explained through the charge model in Figs. 6(a) and 6(b). Na$^+$ ions gain high mobility at high temperature, which leads to Na$^+$ being disordered due to their weak bonding with ions forming a rigid framework [39]. The shift in the Na$^+$ NMR spectra and the disappearance of one Na site were observed for Na$_{3-x}$Ru$_4$O$_9$

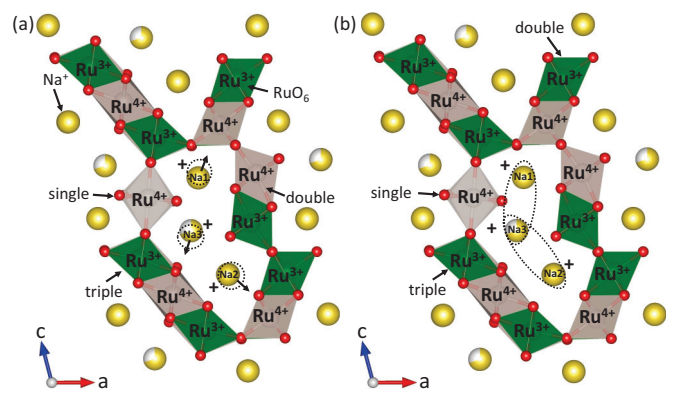FIG. 6. Charge model based on the tunnel structure for Na$_{2.7}$Ru$_4$O$_9$ (a) below the first order transition ($\leqslant T_{C2}$) at room temperature and (b) above the first order transition ($>T_{C2}$) at 450 K. The tunnels are occupied by three different types of Na atoms at different crystallographic sites. The mutual and opposite arrows are showing the displacement of Na$^+$ from their average crystallographic positions as shown by black dashed line circles. Two long elongated black dashed ellipses indicate site sharing.

[37]. Therefore, in Na deficient Na$_{2.7}$Ru$_4$O$_9$, at or above the T_{C2}, one of the Na$^+$ ions moves and shares one of the Na atoms site in the tunnel as shown in Fig. 6(b). The large displacements observed in the SC-XRD data along the b axis favor ionic motions within the tunnels.

As Na$_{2.7}$Ru$_4$O$_9$ has tunnel geometry along the crystallographic b axis with a large cross-section area, a larger number of alkali metal atoms can be accommodated than in Rutile, Ramsdellite, and Hollandite as shown in Fig. 7. This feature makes it attractive in terms of sodium batteries [40] and ion motion related applications [41–44]. Interestingly, formation of the tunnel structure in Na$_{2.7}$Ru$_4$O$_9$ is purely of edge-sharing MO$_6$ octahedra chains [single (1 × 1), double (1 × 2), and triple (1 × 3)], where M is Ru^{3+}/Ru^{4+} and three Na$^+$ cations can reside in those tunnels/channels as shown in Fig. 7(d).

B. Phase transition

The possible prototype HT phase ($a_0 \times b_0 \times c_0$) would be $C2/m$ which is similar to the one reported by Maeno *et al.* [19] as shown in Fig. 3(c). A transition from this HT prototype phase $C2/m$ ($\geqslant 630$ K) to an intermediate phase occurs (630 K $\leqslant$
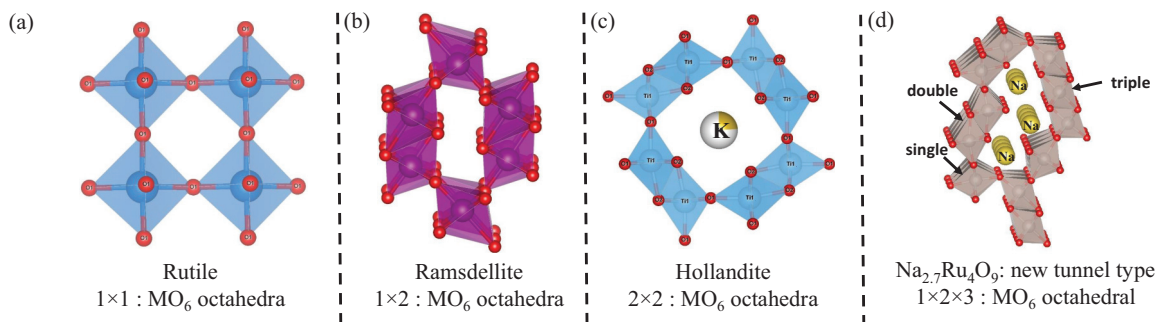

FIG. 7. Comparison of prototype tunnel structures including Na$_{2.7}$Ru$_4$O$_9$ by MO$_6$ octahedra, where M is the transition metal in (a) Rutile, (b) Ramsdellite, and (c) Hollandite type tunnels. (d) An enlarged view is shown of the new tunnel type structure for Na$_{2.7}$Ru$_4$O$_9$ formed by 1 × 2 × 3 edge shared single, double, and triple chains.
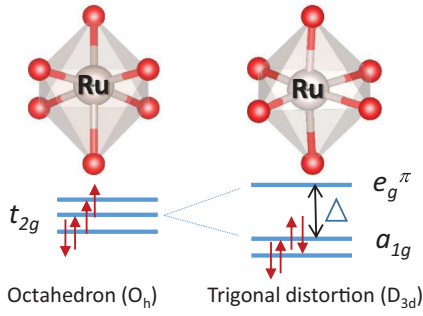
FIG. 8. Schematic representation of the t_{2g} orbital splitting in e_g^π and a_{1g} orbitals caused by trigonal distortion in RuO$_6$ octahedron.

$T \leqslant 365$ K). This intermediate phase transition leads to a doubling ($a_0 \times 2b_0 \times c_0$) of the unit cell from the prototype structure (see Table I, Figs. 3(b), and 5). Below the intermediate phase, a first-order phase transition occurs as confirmed from the resistivity [Fig. 1(a)]. Below 365 K new superlattice peaks appear in the SC-XRD data, which makes the unit cell 18 times ($a_0 \times 6b_0 \times 3c_0$) larger than the prototype phase unit cell (Table I, Figs. 3(b), and 5).

These symmetry lowering structural-phase transitions enlarge the unit cell drastically. Further, from the resistivity behavior it is clear that Fermi surface of the Na$_{2.7}$Ru$_4$O$_9$ is comprised of two types of electrons, (1) itinerant electrons (high spin state of Ru^{3+}/Ru^{4+}) responsible for the metallic behavior and (2) localized electrons (possibly ultralow spin state $t_{2g\uparrow}^2 t_{2g\downarrow}^2$ of Ru^{4+}) mainly responsible for the origin of the first order phase transition. The phase transition originates from the structural transition, which leads to trigonal distortion driven symmetry breaking. In the trigonal distortion, t_{2g} electrons can further split into e_g^π and a_{1g} orbitals and this splitting opens a gap at the Fermi surface (localized electrons of Ru^{4+}). In this case symmetry breaking that would split the 3 t_{2g} levels needs a large crystal-field splitting (Δ) energy as schematically shown by the electronic levels of Ru^{4+} (d^4) in Fig. 8. Therefore, in such a case where electron states are localized, as in the Mott states, the observed $\mathbf{q}_1$ and $\mathbf{q}_2$ modulations in Na$_{2.7}$Ru$_4$O$_9$ may show CO-type modulations due to intersite Coulomb interactions. However, localized charge-ordered states interact with itinerant electrons of Na$_{2.7}$Ru$_4$O$_9$ through SOC and retain the metallicity. IrTe$_2$ is one of the rare examples showing similar behavior with high SOC strength and unconventional CO. In this case, localized spin-orbit Mott states are assisted by Ir^{4+} dimerizations [45]. Thus, the electronic behavior of Na$_{2.7}$Ru$_4$O$_9$ is due to a subtle balance between itinerant and localized electrons [46].

C. Displacement pattern

We now describe the structure and its displaced Ru and Na ions in more detail. Na ions are present at three different crystallographic sites inside the tunnels formed by RuO$_6$ octahedra, as shown in Figs. 6(a) and 6(b). We observe a first-order phase transition with a strong anomaly in the electrical resistance and heat-capacity data. The superstructures have also been observed by SC-XRD for Na$_{2.7}$Ru$_4$O$_9$. This can be understood in terms of the Ru charge ordering, which has been
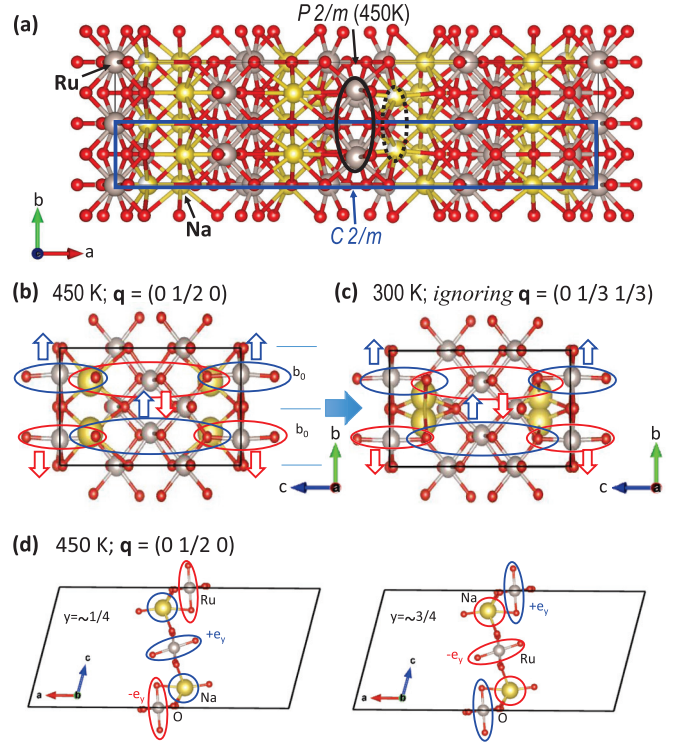

FIG. 9. (a) The $P2/m$ unit cell of Na$_{2.7}$Ru$_4$O$_9$ at 450 K [$\mathbf{q}_1 = (0, \frac{1}{2}, 0)$]. The reference solid blue line represents the HT prototype phase $C2/m$ unit cell. In the $P2/m$ unit cell, black solid and dashed lines vertical ellipses indicate the dimerization of Ru and Na ions along the crystallographic b axis. The displacement pattern of Na ions at (b) 450 K and (c) 300 K in $\mathbf{q}_1 = (0, \frac{1}{2}, 0)$ mode on the bc-plane projection, while (d) ac plane at 450 K is shown at each y layer, 1/4 and 3/4. The blue and red colors in (b)–(d) indicate positive and negative direction shifts.

confirmed by both temperature-dependent bulk and SC-XRD measurements (see Figs. 1 and 2). In order to avoid complexity we ignored the $\mathbf{q}_2 = (0, \frac{1}{3}, \frac{1}{3})$ superlattice reflections and analyzed the displacement patterns by only considering the $\mathbf{q}_1 = (0, \frac{1}{2}, 0)$ superstructure mode with the same unit-cell size and the same space group $P2/m$. The displacement patterns of Na and Ru are shown in Figs. 9(a)–9(d) and Figs. 10(a) and 10(b), respectively. It is worth noting that Ru and Na ions are dimerized in comparison with the HT prototype phase $C2/m$ along the crystallographic b direction as shown by the black solid and dashed vertical ellipses in Fig. 9(a).

From the intermediate phase to the LT phase, the structure shows large Na ion displacements, and one among the three Na sites is displaced along the b direction by about $\frac{1}{4}$ from its normal site. The displaced RuO$_2$ and Na ions are shown by open arrows in Figs. 9(b) and 9(c) in the a-axis projection. This displacement substantially changes the local environment of the structure. The observed large Na$^+$ ion displacements in Na$_{2.7}$Ru$_4$O$_9$ are in good agreement with Fig. 9(d), which shows the b-axis projection of the structure shown in Fig. 9(b) at 450 K. These Na ion displacements greatly affect the electronic structure of Na$_{2.7}$Ru$_4$O$_9$. This leads to displaced Ru ions along the a direction, which forms zigzag chains along the crystallographic c axis for both the intermediate and LT

450 K; **q** = (0 1/2 0) mode

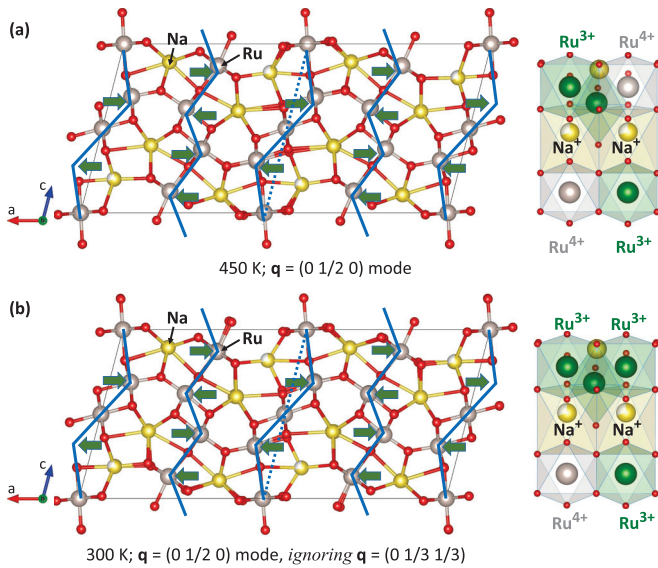300 K; **q** = (0 1/2 0) mode, *ignoring* **q** = (0 1/3 1/3)

FIG. 10. The displacement patterns of Ru ions at (a) 450 and (b) 300 K with $\mathbf{q}_1 = (0, \frac{1}{2}, 0)$ mode on the *ac*-plane projection. The right panel of the figures shows the highly distorted octahedrons local environment of displaced Na ions face sharing with different $Ru^{3+}O_6/Ru^{4+}O_6$ octahedra at (a) 450 and (b) 300 K, respectively.

phases as shown by the filled green arrow in Figs. 10(a) and 10(b), respectively. We observed that due to the shift of the Na ions, Ru^{4+} electrons are favored in the intermediate phase as shown in the right panel of Figs. 10(a) and 10(b). However, Na octahedra sites are highly distorted face sharing with both $Ru^{3+}O_6/Ru^{4+}O_6$ octahedra and Ru atoms form interactions with the alkali ions through oxygen, which stabilize *spd* hybridization. This hybridization strongly influences the 4*d* Ru electrons and the electronic properties of $Na_{2.7}Ru_4O_9$ are greatly affected accordingly. Although such face-sharing sites occur in both the intermediate and LT-phase structures, it is rather unusual to see such a site occupied by an alkali ion, Na, as we find in $Na_{2.7}Ru_4O_9$.

Further, in case of Na disorder driven phase transition, one would expect all Ru ions in the superlattice to show similar charge characteristics below and above the transition, however, it was not observed in $Na_{2.7}Ru_4O_9$. Moreover, the localized Ru

electrons scenario is well supported by the reported Na-NMR on Na deficient $Na_{3-x}Ru_4O_9$ due to Na^+ ion motion [37].

Therefore, the results of a structural investigation by temperature-dependent SC-XRD provide direct evidence for the formation of an unconventional charge ordering (CO). The system remains metallic, but parts of the Fermi surface may lose near the first order phase transition. This then explains the abrupt increase in the experimental resistivity at T_{C2}. Within this scenario the suppression of superlattice peaks above T_{C2} [Fig. 2(c)] can be interpreted as Na^+ ion motions in the $Na_{2.7}Ru_4O_9$ lattice [37] being responsible for the increased localization of 4*d* Ru^{4+} electrons without the loss of metallicity. This scenario is very much consistent with magnetic susceptibility (χ), where short range magnetic correlations were observed. We think that these results are responsible for the origin of the first-order phase transition and provide an unprecedented ionic displacement driven charge ordering in $Na_{2.7}Ru_4O_9$.

To conclude, we have presented evidence for a very unusual charge ordering in $Na_{2.7}Ru_4O_9$ at room temperature while retaining metallicity by combining the results of SC-XRD, electrical resistivity, specific heat, and susceptibility χ (*T*). The temperature-dependent SC-XRD results show superlattice peaks at $\mathbf{q}_1 = (0, \frac{1}{2}, 0)$ and $\mathbf{q}_2 = (0, \frac{1}{3}, \frac{1}{3})$, clear evidence of symmetry breaking with large ionic displacements. This helps most probably establish charge ordering (CO) in $Na_{2.7}Ru_4O_9$. $Na_{2.7}Ru_4O_9$ hosts modest SOC of the Ru mixed valance heavy d^4 ions, which show several unique features such as CO in the metallic state and large alkali metal Na ion displacements in the tunnel lattice. More than one type of electron scattering is involved in the resistivity, alternatively making this material a uniquely suitable example for several possible advanced applications such as in ion transport quantum computers and future energy storage materials. Further, the higher value of γ indicates that $Na_{2.7}Ru_4O_9$ belongs to the class of strongly correlated electron systems.

[1] S. Sachdev, *Quantum Phase Transitions*, 2nd ed. (Cambridge University Press, Cambridge, England, 2011).

[2] J. Goldstone, A. Salam, and S. Weinberg, Phys. Rev. **127**, 965 (1962).

[3] P. Zhou, C. Q. Sun, and L. Z. Sun, Nano Lett. **16**, 6325 (2016).

[4] J. P. Carlo, T. Goko, I. M. Gat-Malureanu, P. L. Russo, A. T. Savici, A. A. Aczel, G. J. MacDougall, J. A. Rodriguez, T. J. Williams, G. M. Luke, C. R. Wiebe, Y. Yoshida, S. Nakatsuji, Y. Maeno, T. Taniguchi, and Y. J. Uemura, Nat. Mater. **11**, 323 (2012).

[5] Seongsu Lee, J.-G. Park, D. T. Adroja, D. Khomskii, S. Streltsov, K. A. McEwen, H. Sakai, K. Yoshimura, V. I. Anisimov, D. Mori, R. Kanno, and R. Ibberson, Nat. Mater. **5**, 471 (2006).

[6] S. A. J. Kimber, J. A. Rodgers, H. Wu, C. A. Murray, D. N. Argyriou, A. N. Fitch, D. I. Khomskii, and J. P. Attfield, Phys. Rev. Lett. **102**, 046409 (2009).

[7] S. A. J. Kimber, M. S. Senn, S. Fratini, H. Wu, A. H. Hill, P. Manuel, J. P. Attfield, D. N. Argyriou, and P. F. Henry, Phys. Rev. Lett. **108**, 217205 (2012).

[8] S. Lee, J. R. Zhang, S. Torii, S. Choi, D.-Y. Cho, T. Kamiyama, J. Yu, K. A. McEwen, and J.-G. Park, J. Phys.: Condens. Matter **25**, 465601 (2013).

[9] S. A. J. Grigera, R. S. Perry, A. J. Schofield, M. Chiao, S. R. Julian, G. G. Lonzarich, S. I. Ikeda, Y. Maeno, A. J. Millis, and A. P. Mackenzie, Science **294**, 329 (2001).

[10] M. Freamat, X. N. Lin, V. Durairaj, S. Chikara, G. Cao, and J. W. Brill, Phys. Rev. B **72**, 014458 (2005).

[11] D. N. Basov, R. D. Averitt, D. van der Marel, M. Dressel, and K. Haule, Rev. Mod. Phys. **83**, 471 (2011).

[12] K. Miyake and O. Narikiyo, Phys. Rev. lett. **83**, 1423 (1999).

[13] C. Sekine, T. Uchiumi, I. Shirotani, and T. Yagi, Phys. Rev. Lett. **79**, 3218 (1997).

[14] V. Durairaj, X. N. Lin, Z. X. Zhou, S. Chikara, E. Ehami, A. Douglass, P. Schlottmann, and G. Cao, Phys. Rev. B **73**, 054434 (2006).

[15] G. Cao, X. N. Lin, L. Balicas, S. Chikara, J. E. Crow, and P. Schlottmann, New J. Phys. **6**, 159 (2004).

[16] G. Cao, X. N. Lin, S. Chikara, V. Durairaj, and E. Elhami, Phys. Rev. B **69**, 174418 (2004).

[17] P. Khalifah, K. D. Nelson, R. Jin, Z. Q. Mao, Y. Liu, Q. Huang, X. P. A. Gao, A. P. Ramirez, and R. J. Cava, Nature (London) **411**, 669 (2001).

[18] J. M. Longo, P. M. Raccah, and J. B. Goudenough, J. Appl. Phys. **39**, 1327 (1968).

[19] Y. Maeno, H. Hashimoto, K. Yoshida, S. Nishizaki, T. Fujita, J. G. Bednorz, and F. Lichtenberg, Nature (London) **372**, 532 (1994).

[20] R. A. Borzi, S. A. Grigera, J. Farrell, R. S. Perry, S. J. S. Lister, S. L. Lee, D. A. Tennant, Y. Maeno, and A. P. Mackenzie, Science **315**, 214 (2007).

[21] C. Lester, S. Ramos, R. S. Perry, T. P. Croft, R. I. Bewley, T. Guidi, P. Manuel, D. D. Khalyavin, E. M. Forgan, and S. M. Hayden, Nat. Mater. **14**, 373 (2015).

[22] A. W. Rost, R. S. Perry, J. F. Mercure, A. P. Mackenzie, and S. A. Grigera, Science **325**, 1360 (2009).

[23] Z. Q. Mao, M. Zhou, J. Hooper, V. Golub, and C. J. O'Connor, Phys. Rev. Lett. **96**, 077205 (2006).

[24] G. Cao, L. Balicas, W. H. Song, Y. P. Sun, Y. Xin, V. A. Bondarenko, J. W. Brill, S. Parkin, and X. N. Lin, Phys. Rev. B **68**, 174409 (2003).

[25] T. Vogt, E. Schweda, C. Wustefeld, J. Strahle, and A. K. Cheetham, J. Solid State Chem. **83**, 61 (1989).

[26] M. L. Carter and R. L. Withers, J. Solid State Chem. **178**, 1903 (2005).

[27] J. M. D. Coey, M. Viret, and S. von Molnár, Adv. Phys. **48**, 167 (1999).

[28] J. B. Goodenough, Phys. Rev. **100**, 564 (1955).

[29] E. E. Rodriguez, T. Proffen, A. Llobet, J. J. Rhyne, and J. F. Mitchell, Phys. Rev. B **71**, 104430 (2005).

[30] J. Rodríguez-Carvajal, Physica B: Condensed Matter **192**, 55 (1993).

[31] A. P. Pikul, D. Kaczorowski, T. Plackowski, A. Czopnik, H. Michor, E. Bauer, G. Hilscher, P. Rogl, and Y. Grin, Phys. Rev. B **67**, 224417 (2003).

[32] See Supplemental Material at http://link.aps.org/supplemental/10.1103/PhysRevB.98.085113 for information on the electrical resistivity (ρ) fitting by Bloch-Grneisen-Mott (BGM) model (SM-1), single crystal XRD refinement (SM-2), and complementary magnetization results (SM-3).

[33] E. S. R. Gopal, *Specific Heats at Low Temperatures* (Plenum, New York, 1966).

[34] A. Krimmel, A. Günther, W. Kraetschmer, H. Dekinger, N. Büttgen, A. Loidl, S. G. Ebbinghaus, E.-W. Scheidt, and W. Scherer, Phys. Rev. B **78**, 165126 (2008).

[35] K. A. Regan, Q. Huang, M. Lee, A. P. Ramirez, and R. J. Cava, J. Sol. Stat. Chem. **179**, 195 (2006).

[36] G. Cao, S. McCall, F. Freibert, M. Shepard, P. Henning, and J. E. Crow, Phys. Rev. B **53**, 12215 (1996).

[37] Y. Onoda, S. H. Chung, A. Watanabe, and T. Mitsuhashi, Solid State Ionics **136**, 365 (2000).

[38] M. L. Foo, Y. Wang, S. Watauchi, H. W. Zandbergen, T. He, R. J. Cava, and N. P. Ong, Phys. Rev. Lett. **92**, 247001 (2004).

[39] Y. H. Kim, P. Arunkumar, B. Y. Kim, S. Unithrattil, E. Kim, S.-Y. Moon, J. Y. Hyun, K. H. Kim, D. Lee, J.-S. Lee, and W. B. Im, Nat. Mater. **16**, 543 (2017).

[40] N. Yabuuchi, M. Kajiyama, J. Iwatate, H. Nishikawa, S. Hitomi, R. Okuyama, R. Usui, Y. Yamada, and S. Komaba, Nat. Mater. **11**, 512 (2012).

[41] F. Chen, J. M. Pringle, and M. Forsyth, Chem. Mater. **27**, 2666 (2015).

[42] V. A. Nikitina, S. S. Fedotov, S. Yu. Vassiliev, A. S. Samarin, N. R. Khasanova, and E. V. Antipova, J. Electrochem. Soc. **164**, A6373 (2017).

[43] B. Lekitsch, S. Weidt, A. G. Fowler, K. Molmer, S. J. Devitt, C. Wunderlich, and W. K. Hensinger, Sci. Adv. **3**, e1601540 (2017).

[44] D. Kielpinski, C. Monroe, and D. J. Wineland, Nature (London) **417**, 709 (2002).

[45] K.-T. Ko, H.-H. Lee, D.-H. Kim, J.-J. Yang, S.-W. Cheong, M. J. Eom, J. S. Kim, R. Gammag, K.-S. Kim, H.-S. Kim, T.-H. Kim, H.-W. Yeom, T.-Y. Koo, H.-D. Kim, and J.-H. Park, Nat. Commun. **6**, 7342 (2015).

[46] M. A. Subramanian and A. W. Sleight, Solid State Sci. **4**, 347 (2002).